ACS OMEGA

Article

Cite This: ACS Omega 2018, 3, 16976−16988

http://pubs.acs.org/journal/acsodf

Rational Design of Efficient Environmental Sensors: Ring-Shaped Nanostructures Can Capture Quat Herbicides

Ángel Vidal-Vidal,[†] Enrique M. Cabaleiro-Lago,[‡] Carlos Silva López,[*,†] and Olalla Nieto Faza[*,§]

[†]Departamento de Química Orgánica, Facultade de Química, Campus Lagoas-Marcosende, 36310 Vigo, Spain

[‡]Departamento de Química Física, Facultade de Ciencias, Campus de Lugo, Avda. Alfonso X El Sabio s/n, 27002 Lugo, Spain

[§]Departamento de Química Orgánica, Universidade de Vigo, Campus As Lagoas, 32004 Ourense, Spain

Supporting Information

ABSTRACT: The viability of using [*n*]-cycloparaphenylenes (CPPs) of different sizes to encapsulate diquat (DQ) pesticide molecules has been tested analyzing the origin of the host−guest interactions stabilizing the complex. This analysis provides rational design capabilities to construct ad hoc capturing systems tailored to the desired pollutant. All CPPs considered (n = 7−12) are capable of forming remarkably stable complexes with DQ, though [9]-CPP is the best candidate, where a fine balance is established between the energy penalty due to the deformation + repulsion of the pesticide molecule inside the cavity (larger in smaller CPPs) and the maximization of the favorable dispersion, electrostatic and induction contributions (which also decrease in larger rings). These encouraging results prompted us to evaluate the potential of using Resonance Raman spectroscopy on nanohoop complexes as a tool for DQ sensing. The shifts observed in the vibrational frequencies of DQ upon complexation allow us to determine whether complexation has been achieved. Additionally, a large enhancement of the signals permits a selective identification of the vibrational modes.

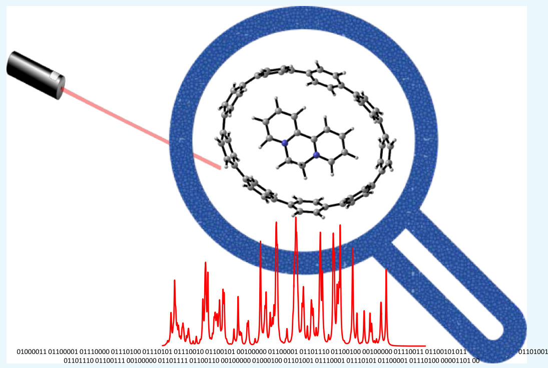

1. INTRODUCTION

A pesticide can be defined as any substance intended to prevent, control, or destroy any pest that causes damage or interferes with the production, processing, storage, transport, or commercialization of foodstuffs. The use of pesticides is a hotly debated topic.[1−4] Defenders usually appeal to various benefits such as control of pests and plant disease vectors, a fact that leads to improved crop yields, better crop quality, and control of harmful invasive species. The control of losses in crop production improves the harvest, which leads not only to farm and agribusiness revenues, increased export returns, and, in general, an economic activation of the primary sector, but also to higher arable land productivity ratios. Pesticides also allow us to control organisms that harm obtaining wood from trees, shrubs, leaves, or resins. Lastly, the use of pesticides is of vital importance for the control of human/livestock disease vectors and nuisance organisms, a fact that has reduced the number of deaths and human and animal suffering across the planet.

However, there are also numerous drawbacks related to the use of pesticides. The use of chemical substances for the control of pests is inextricable with associated risks to the environment, workers, and consumers that are increased by their indiscriminate use and bad in situ applications. It must be kept in mind that once applied, pesticides do not stay put and can pollute the environment. Some authors indicate that over 98% of aerial and terrestrial sprayed insecticides and around 95% of herbicides reach a destination other than their target species and end up in the air, surface or ground water, soil, food-chain, and so forth.[4] Some consequences are the reduction of biodiversity, the contribution to pollinator decline, and the decrease of the quality of fresh water. Perhaps, the two issues producing most concerns in this field are the emergence of resistance (resulting in the need of higher concentrations or the development of new, more aggressive, compounds) and damage to human health. Resistance to pesticides is a large scale problem that can develop in a very short period of time. In terms of public health, pesticides may cause both acute and delayed health effects in people who are regularly exposed to them. It should be noted that in many cases pesticide metabolites are more toxic and persistent than the original molecule.

In this work, we will focus on herbicides, more specifically in the family of quaternary ammonium compounds, better known as quats. There are numerous molecules belonging to this family available on the market such as cyperquat, mepiquat, chlormequat, and difenzoquat although, perhaps, the best known and widely used in the world are paraquat [PQ] and diquat [DQ] (6,7-dihydrodipyrido[1,2-*a*:2′,1′-*c*]pyrazine-5,8-diium). Some of the crops in which these herbicides are used

Received: October 6, 2018
Accepted: November 27, 2018
Published: December 11, 2018

are beet, soybeans, grapevines, alfalfa, sugar beet, and potato.[5] Quats are known to act on photosystem I, which produces free electrons to drive photosynthesis. The free electrons of photosystem I react with pesticide ions leading to free radicals that are rapidly converted by oxygen into superoxides. These highly reactive superoxides attack unsaturated fatty acids of the membranes, causing a rapid disintegration of cells and tissues,[6−8] that result in loss of water and rapid drying.

According to the PPDB (pesticide properties database),[5] the DQ has an oral lethal dose (LD_{50}) of 214 mg/kg, approximately twice that of the PQ: 110 mg/kg.[5,9] In terms of their fate in the environment, both have low volatility and low leachability and high potential to bind to particles. For DQ, its DT_{50} factor (soil degradation in aerobic conditions) is 2345 days and it exhibits moderately fast aqueous photolysis (DT_{50} = 7 days) at pH = 7, but is stable to aqueous hydrolysis.[10] On the basis of these data, quats can be considered very persistent compounds in the environment and difficult to eliminate. At the time of writing of this manuscript, the legal status of quats in the European Union is diverse. DQ, mepiquat and chlormequat are currently authorized substances, whereas, for example, PQ is excluded as an active substance and absent in the list of active substances of plant protection products (EC 1107/2009). Although PQ has been banned others are not, and because of their persistence at rather high levels in the environment coupled to their moderate to high toxicity for humans, birds, algae and aquatic invertebrates,[9] it seems necessary to explore new elimination methods. Because of its toxicity, persistence, and approval for agricultural purposes and it being one of the most used pesticides in its family, DQ is going to be used as a model quat pesticide in this study.

The actual problem in this endeavor is not usually the actual degradation of organic pollutants, as procedures abound for this task, but how to agglutinate the remains of pesticides dispersed through different and extended matrices to perform the elimination. Currently, methods based on the use of supramolecular chemistry are becoming increasingly important in agriculture, not only for the elimination of contaminants but also for the controlled release of certain phytosanitary substances.[11−15] Some of the systems that can be used for the capture of organic molecules are metal organic frameworks,[16,17] calixarenes,[18,19] cucurbiturils,[20,21] bambusurils,[22] cyclodextrins,[11,14] and covalent organic frameworks[23] among others.

As a capturing device in this in silico study, we propose the use of nanohoops ([*n*]-cycloparaphenylenes) because of their binding capacity, their useful spectroscopic properties, and their accessibility, due to the recent development of different methods for their synthesis.

[*n*]-cycloparaphenylenes ([*n*]-CPPs) were termed in 2008 as carbon nanohoops by Jasti and Bertozzi after the first synthesis was accomplished.[24] In solid state, nanohoops form a rigid three-dimensional architecture with long-range channels[25−28] stabilized by multiple $\pi-\pi$ contacts.[29,30] The closed ring structure provides the [*n*]-CPPs with several advantageous properties in relation to their linear counterparts, such as a narrowing of the HOMO−LUMO gap,[31] and diameter-dependent fluorescence,[29,32,33] electrochemical,[34,35] and opto-electronic properties[32,36−38] that can be exploited in sensing applications.

Nanohoops possess a unique, rigid, full sp^2-hybridized conjugated core with a radially oriented π system[31] which provides a hydrophobic electron-rich cavity that can act as a strong host for electron-deficient guests.[39−42] CPP size can be tuned spanning a range suitable for encapsulating small molecules such as CO_2[43] or species as large as fullerenes (C_{60}, C_{70}, C_{82}...).[39−42,44−46] The encapsulating properties of these systems however are still to be rigorously studied. The present work opens the door to complexations and even selective separations that can be optimized by changing the nature of the nanoring through chemical modification, thus creating fine-tuned donor−acceptor nanohoop structures.

A recent effort to characterize the sensing capability of CPPs to detect ammonium species was carried out by Gaeta and coworkers.[47] In this work, a systematic experimental study on the complexation ability of [8]-CPP and various pyridinium ions was performed. [8]-CPP was found to act as an excellent host for smaller pyridinium ions but it fails when PQ is tested. Gaeta hypothesizes that the larger size of PQ could be responsible for [8]-CPP failing to host this pesticide. These recent results are however promising and led us to undertake a thorough study on the potential of these macrocyclic structures to sense and capture quats. Because PQ has been banned from agricultural use in the European Union we focused our attention on DQ, a pesticide that is currently in use and has similar structure and effects, but features a smaller molecular size.

With this work, we intend to answer, among other, the following questions:

- Is it possible to complex big pyridinium cations inside a nanohoop? If possible, how stable are these complexes?
- What size of ring is necessary to maximize the stabilizing host−guest interactions?
- Can nanohoops act as sensing-devices for the efficient detection of quats?
- Can vibrational spectroscopy be used as a detection tool? If possible, what is the most promising technique?

2. COMPUTATIONAL METHODS

Density functional theory (DFT) in the Kohn−Sham formulation as implemented in Gaussian 09[48] was used to locate minimum structures on the potential energy surfaces of the complexes under study. All calculations were performed with the hybrid-meta GGA functional M06-2X in combination with the Def2SVP Ahlrich's split-valence quality basis. The M06-2X functional was selected because of its recognized good performance in the study of hydrogen bonds, H−π, $\pi-\pi$ and electrostatic interactions both in neutral and charged dimeric systems.[49,50] To achieve results with high accuracy, tight self-consistent field criteria and a fine-pruned grid for the numerical integration were used (the latter containing 99 radial points and 590 angular points per shell). Harmonic analysis of the second derivatives of the energy with respect to the nuclear displacements was also computed for each stationary point to ensure that a minimum structure and not a transition state or higher order saddle point was located.

Before any molecular structure can be used as a sensor, an initial step of association is needed. Solvation effects however can play an important role in this association step. In general, liberation of solvent molecules inside the cavity of the host dominates the host−guest complex formation because of entropic effects. Owing to the constant size of the DQ guest studied in this work, the same number of solvent molecules is expected to be expelled from the cavity of the host,

DOI: 10.1021/acsomega.8b02673
ACS Omega 2018, 3, 16976−16988

irrespectively of the size of the cavity. For this reason, the gas phase process is described in this work, because the main interest of this study is the accurate description of the host−guest interactions, key to molecular recognition and sensing. Nevertheless, other energy terms can disfavor the complexation process when it occurs in solvent phase, which should be taken into account. Fortunately, binding energies in solution can be estimated efficiently via a continuum solvation approach, such as PCM.[51−53] Interaction host−guest energies have therefore been computed in various solvents of increasing polarity (see the Supporting Information). In all cases, the host−guest complex formation is favorable. Also, the entry of DQ in the cavity of the nanohoops may be kinetically penalized. We have estimated the barrier for such process through a rigid scan (see Supporting Information) to be about 10 kJ/mol, a low value for a process that is expected to occur at room temperature.

Interaction energies for the complexes under study were computed by means of the supermolecule method using the counterpoise procedure to avoid basis set superposition errors. Interaction energies for the case of two interacting molecules can be written as

$$\Delta E_{\mathrm{int}} = E_{\mathrm{AB}}^{\mathrm{dimer}}(\mathrm{AB}) - E_{\mathrm{A}}^{\mathrm{dimer}}(\mathrm{AB}) - E_{\mathrm{B}}^{\mathrm{dimer}}(\mathrm{AB}) \tag{1}$$

with terms in parentheses indicating the basis set, subscripts the system under consideration and superscripts the structure of the unit employed in the calculation. As the geometry of the molecules change when the complex is formed, an additional contribution to the energy describing this effect (deformation energy) must be included. It is obtained as the difference in energy between the molecules in the cluster geometry and isolated

$$E_{\mathrm{def}} = \sum_i \left(E_i^{\mathrm{clus}}(i) - E_i^{\mathrm{isolated}}(i)\right) \tag{2}$$

Finally, the complexation energy of the system can be written as a combination of both terms: interaction and deformation energy.

$$\Delta E_{\mathrm{complex}} = \Delta E_{\mathrm{int}} + E_{\mathrm{def}} \tag{3}$$

Symmetry-adapted perturbation theory (SAPT)[54,55] can be used to make a decomposition of the previous interaction energy into physically meaningful components such as electrostatic, exchange, induction, and dispersion. In SAPT, the total Hamiltonian of the system is written as

$$\hat{H} = \hat{F}^{\mathrm{A}} + \hat{F}^{\mathrm{B}} + \xi\hat{W}^{\mathrm{A}} + \eta\hat{W}^{\mathrm{B}} + \zeta\hat{V} \tag{4}$$

where $\hat{F}^{\mathrm{A}}$ and $\hat{F}^{\mathrm{B}}$ are the monomer Fock operators and $\hat{W}^{\mathrm{A}}$ and $\hat{W}^{\mathrm{B}}$ are the Møller−Plesset fluctuation operators for fragments A and B, respectively. $\hat{V}$ consists of the intermolecular Coulomb operator and can be written as follows

$$\begin{aligned}\hat{V} &= \sum_{i\in \mathrm{A}}\sum_{j\in \mathrm{B}} \hat{\nu}(ij)\\ &= \sum_{i\in \mathrm{A}}\sum_{j\in \mathrm{B}} \frac{1}{|\vec{r}_i - \vec{r}_j|} + \frac{\hat{\nu}_{\mathrm{A}}(j)}{N_{\mathrm{A}}} + \frac{\hat{\nu}_{\mathrm{B}}(j)}{N_{\mathrm{B}}} + \frac{V_0}{N_{\mathrm{A}}N_{\mathrm{B}}}\end{aligned} \tag{5}$$

where V_0 is the nuclear interaction energy between the two fragments and $\hat{\nu}_{\mathrm{A}}(j)$ describes the interaction of electron $j \in \mathrm{B}$ with nucleus $I \in \mathrm{A}$ ($\hat{\nu}_{\mathrm{B}}(i)$ has an equivalent meaning). The SAPT approach is based on the Rayleigh−Schrødinger perturbation expansion with respect to perturbation parameters ξ, ζ, and η. The resulting interaction energy can be expressed as

$$\Delta E_{\mathrm{int}} = \sum_{i=1}^{\infty}\sum_{j=0}^{\infty} \left(E_{\mathrm{pol}}{}^{(ij)} + E_{\mathrm{exch}}{}^{(ij)}\right) \tag{6}$$

where i indicates the order in perturbation theory with respect to the intermolecular potential and j indicates the order with respect to the intramolecular electron correlation. Usually, attractive terms (electrostatic, induction, and dispersion) are originated from the polarization expansion while repulsive terms arise from the use of a global antisymmetrizer to force the correct permutational symmetry of the dimer wavefunction.

The SAPT series can be truncated according to the desired accuracy. The simplest SAPT method is called SAPT0, an approach that truncates the expansion series in second order. This method essentially treats the monomers at the HF level (intramolecular electron correlation is neglected) and dispersion terms arise from second-order perturbation theory. The different terms of the SAPT0 energy equation are grouped according to their nature (electrostatic, repulsion, induction, and dispersion) following the proposal of Parker et al.[55] using a color code. The blue represents electrostatic terms, red shows the repulsive component, inductive terms are written in green, and in pink the dispersive contributions. The global SAPT0 energy is given by the equation:

$$\begin{aligned}\mathrm{SAPT0} &= E_{\mathrm{elect}}{}^{(10)} + E_{\mathrm{exch}}{}^{(10)} + \delta E_{\mathrm{HF}}{}^{(2)} + E_{\mathrm{ind},r}{}^{(20)}\\ &\quad + E_{\mathrm{exch-ind},r}{}^{(20)} + E_{\mathrm{exch-disp}}{}^{(20)} + E_{\mathrm{disp}}{}^{(20)}\end{aligned} \tag{7}$$

In this equation, the superscripts v,w in the terms E^{vw} define the order in $\hat{V}$ and in $\hat{W}^{\mathrm{A}} + \hat{W}^{\mathrm{B}}$, respectively, and the subscripts "r" indicate that the response correction for induction is incorporated by solving coupled-perturbed HF equations.[56,57] The Hartree−Fock correction $\delta E_{\mathrm{HF}}{}^{(2)}$ represents polarization beyond the second order $E_{\mathrm{ind}}{}^{20}$ and is defined as

$$\begin{aligned}\delta E_{\mathrm{HF}}{}^{(2)} &= \Delta E_{\mathrm{int\,,supermolecule}}^{\mathrm{HF}} - (SAPT0)\\ &\quad + \left(E_{\mathrm{exch-disp}}{}^{(20)} + E_{\mathrm{disp}}{}^{(20)}\right)\end{aligned} \tag{8}$$

where $\Delta E_{\mathrm{int,supermolecule}}^{\mathrm{HF}}$ is the interaction energy at the HF level computed following the supermolecule approach.

To deepen in the study of the DQ complexation with nanohoops, the interaction energy of the DQ-[n]-CPP complex has been fragmented according to different chemical groups using F-ISAPT0.[58−61] Within this methodology, it is possible to analyze the contribution to the global interaction energy coming from each defined fragment. All calculations related to the SAPT methodology have been carried out with the PSI4 software,[62] benefiting from the density-fitting approach. This procedure introduces negligible errors into the SAPT energy and greatly improves efficiency. In all cases, the basis set jun-cc-pVDZ[63] as recommended by Sherril has been used with the corresponding auxiliary basis (jun-cc-pVDZ-ri and jun-cc-pVDZ-jkfit) to make use of the density-fitting approach. Jun-cc-pVDZ basis set is created removing diffuse functions (diffuse from H and He and also the highest angular momentum diffuse function from the rest of the atoms) from the well-known Dunning's correlation consistent basis set: aug-cc-pVDZ.[64] Once the F-ISAPT computation is done, the SAPT0 analysis shown along the results section is obtained as a sum of all the chemical group contributions.

DOI: 10.1021/acsomega.8b02673
ACS Omega 2018, 3, 16976−16988

In order to gather a deeper insight into the type of interactions present in the complexes under study, a noncovalent interaction analysis is performed using for this purpose the Multiwfn program.[65] The noncovalent interaction index (NCI) identifies interactions in a chemical system based solely on the electron density and its derivatives.[66] This method is based on the peaks that appear in the reduced density gradient (RDG) at low densities enabling the identification of favorable and unfavorable noncovalent interactions.

$$\mathrm{RDG}\ (r) = \frac{1}{2(3\pi^2)^{1/3}}\frac{|\nabla\rho(\mathbf{r})|}{\rho(\mathbf{r})^{4/3}} \tag{9}$$

To discriminate the type of interactions, low-density and low-gradient regions cannot be used alone,[66] and for this reason the sign of the second Hessian eigenvalue (λ_2) times the electron density (ρ) is used to distinguish bonded from nonbonded interactions and also to yield a measure of their relative strength. A BGR color scale where blue indicates strongly attractive interactions, green weak van der Waals (vdW) interactions, and red strongly repulsive interactions is used to map out the sign $\lambda_2\rho$ product onto the 0.4 a.u. RDG isosurface. A RDG versus the sign(λ_2)ρ scatter graph is also computed as a complementary way to visualize and confirm the type of interactions and their intensity as a function of the chosen isosurface.

To analyze the possibility that these supramolecular complexes can be also used as sensing devices, resonance Raman (RR) spectroscopy is proposed as a detection tool. To simulate Raman pre-resonance conditions, first the UV–vis spectrum is computed using time-dependent DFT considering 50 different excited states. Those transitions from the ground state that have the larger oscillator strengths are usually chosen as incident frequencies; nevertheless, the calculation of the frequency-dependent polarizabilities can diverge at exact resonance conditions. There are two main ways to solve the divergence problem: the use of a small detuning of the excitation frequency[67,68] or the incorporation of a damping parameter into the frequency-dependent polarizability expression.[69] In this work, we have performed a detailed analysis of the effect of the excitation wavelength on the Raman activity spectra of the optimal DQ–CPP complex computing its 3D RR spectrum. Exact resonance conditions were avoided in all cases, so no damping parameter was used for the calculation. The frequency-dependent polarizabilities and subsequently the Raman activities were calculated using the coupled perturbed DFT theory as implemented in the Gaussian09 software package, and the final spectrum was represented using a Lorentzian band shape with a half-width at half height of 4 cm^{-1}.

3. RESULTS AND DISCUSSION

In a first step, host–guest complexes between DQ and different size CPPs were obtained. To account for the conformational flexibility of DQ inside the CPP macromolecule, different orientations were considered for the guest and subjected to unconstrained geometry optimizations. The resulting structures were screened according to their relative energy, selecting the most stable complex for each size of CPP to carry out the subsequent analysis (Figure 1).

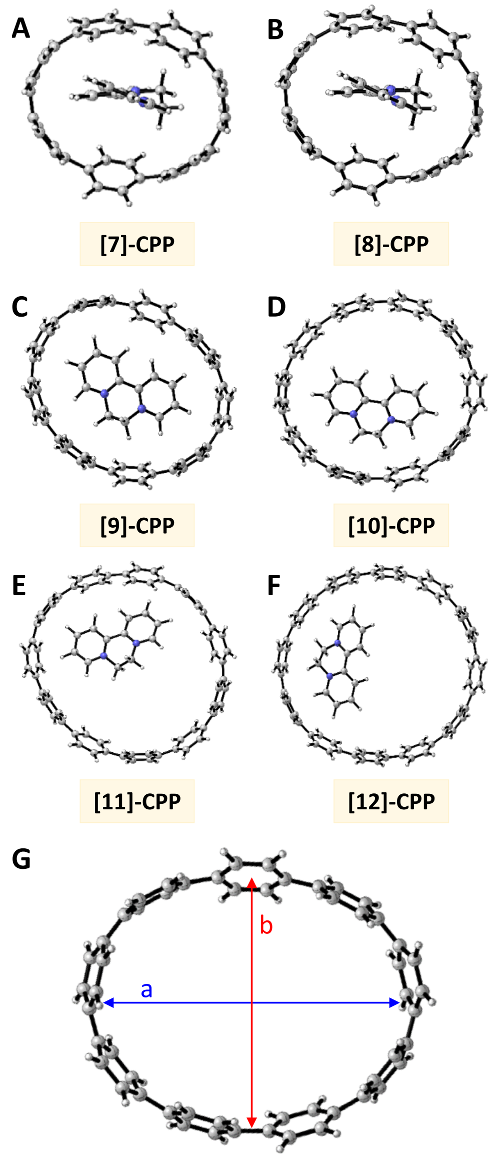

Figure 1. Minimum energy CPP@DQ configurations are shown for systems with increasing CPP ring-sizes, ranging between 7 and 12 benzene rings (A–F). Subfigure (G) illustrates the geometric parameters considered for the characterization of the cavity inside the nanohoop. The elliptical parameters *a* and *b* for each of these structures are collected in Table 1.

Once the structures of the systems were obtained the interaction, complexation and deformation energies have been calculated as described in the Computational Methods section.

As shown in Table 1, complexation energies vary between −190 and −258 kJ/mol, approximately. If the complexation energy is analyzed as a function of size, a clear minimum appears: the nanohoop formed by 9 benzene rings ([9]-CPP) with a complexation energy of −257.61 kJ/mol is the most stable one. The second largest complexation energy is found for [10]-CPP (E_{int} = −228.53 kJ/mol) followed by [8]-CPP (E_{int} = −223.17 kJ/mol). These results reveal that there is a very favorable interaction between DQ and the nanoring structure for the entire series of nanohoops, even if the formation of each of these complexes involves an energy penalty due to the deformation of the interacting species with respect to their isolated geometry. As it can be seen in Table 1,

DOI: 10.1021/acsomega.8b02673
ACS Omega 2018, 3, 16976−16988

Table 1. Energy Components in the Formation of DQ@[n]-CPP Host−Guest Complexes[a]

system	$N = 7$	$N = 8$	$N = 9$	$N = 10$	$N = 11$	$N = 12$
E_{com}	−210.62	−223.17	−257.61	−228.53	−189.66	−207.90
E_{int}	−234.89	−255.81	−284.22	−237.69	−202.67	−222.17
E_{def}	24.27	32.64	26.61	9.16	13.01	14.27
E_{def} (CPP)	22.47	29.29	25.69	8.37	11.00	13.56
E_{def} (DQ)	1.84	3.31	0.92	0.79	2.01	0.71
init. size	9.54	10.83	12.32	13.65	15.08	16.42
a	10.4	11.61	13.58	14.01	15.81	17.54
b	8.58	10.44	10.8	13.16	14.41	15.11
f	0.18	0.10	0.20	0.06	0.09	0.14

[a]Interaction, complexation, and deformation energies (in kJ/mol) are shown in the first three entries of the table. The total deformation energy is dissected in [n]-CPP and DQ contributions. Initial nanohoop size shows its diameter when isolated (in Å, circular cavity). Finally, elliptical parameters a and b (Å) correspond to the major and minor axis of the CPP cavity when complexed with DQ. Flattening parameter (f) measures the compression of the ellipse and it is defined as $f = (a - b)/a$.

these deformation energies range between 9.16 kJ/mol for [10]-CPP and 32.64 kJ/mol for [8]-CPP and are dominated by the deformation of the CPP moiety. In all cases, the geometrical changes of the nanohoop upon complexation contribute more than 84% of the total deformation energy and deformation energies of DQ only account for 0.71−3.31 kJ/mol.

Without taking into account the deformation energy necessary to form the supramolecular system, the interaction energies range between −202 and −284 kJ/mol. The trend is the same found for complexation energies, although DQ@[8]-CPP has a larger interaction energy than DQ@[10]-CPP. The increased interaction due to the closer contact favored by the smaller ring-size in the former is compensated by the highest deformation energy for both the nanohoop and DQ, leading to a less favorable complexation. Thus, the interplay between interaction and deformation energies is key in determining the most stable DQ@[n]-CPP complexes, and deformation of the nanohoop is the largest contributor. Isolated nanohoops feature mostly cylindrical cavities; however, when complexed with DQ, the nanoring adopts an ellipse-like shape. The [9]-CPP system, when forming a complex with DQ, increases its size by 1.48 Å in one axis and decreases it by 1.22 Å in the other (a percentage variation of +9.8 and −12.1%, respectively, with respect to empty [9]-CPP), which is reflected in the second greatest deformation energy. However, this deformation is invested in a better degree of adjustment of the guest into the cavity, enhancing the vdW interactions so that DQ@[9]-CPP has the largest interaction and complexation energies in the series. Actually, [9]-CPP is the smallest system in which DQ fits sideways inside, that is, establishing C−H−π contacts with the nanoring (this is associated with a high flattening parameter f of 0.20).

In the case of [7]-CPP and [8]-CPP, the cavity is too small to allow a flat layout of the guest molecule, which is then forced to adopt a perpendicular arrangement to the ring, establishing in this case stacking-type interactions (see Figure 1). This spatial arrangement explains why in [8]-CPP, axial deformations of just 0.35 and 0.74 Å are observed. Among the systems under study, the relatively large structural variations found in [12]-CPP (1.31 and −1.12 Å, in each of the axes) are especially interesting because this nanohoop is big enough to host two guest molecules (see Figure 1). The average percentage change is around 7.40% but the energy penalty associated to this deformation is only 13.56 kJ/mol. This fact can be attributed to the larger flexibility of the macromolecule, which allows it to maximize the host−guest interactions at a reduced cost. Hence, the relatively high flattening parameter (f = 0.14). It is worth noticing that the interaction energies are lower in larger rings as many short-range interactions between the guest and the host are lost. The spatial arrangement of DQ inside [12]-CPP precludes stabilizing contacts that could be established between half of the DQ molecule and cycloparaphenylene. The great difference between the capturing efficiency of the 9- and 10-membered nanorings can be attributed to the loss of these stabilizing short range intermolecular interactions. Because weak vdW interactions are highly dependent on distance, a larger void space in the [10]-CPP cavity causes loss of effectiveness in host−guest interactions.

Weak stabilizing interactions in host−guest complexes can be visualized by analyzing noncovalent interactions as shown in Figure 2. In this figure, RDG values versus the electron density multiplied by the sign of the second eigenvalue of the hessian are displayed. This produces a scatter plot where the falling tails represent noncovalent interactions, and their color code provides the kind of interaction (repulsive, weakly attractive or strongly attractive, the last one usually associated to hydrogen bonds). The abundance of points forming a tail in the region around zero (represented in green) highlights the existence of numerous weak interactions. The points in red correspond to steric repulsive interactions. These are located at the geometric center of each benzene ring of the nanohoop, they are intramolecular steric contacts and therefore do not affect the interactions with the guest molecule. In fact, we found no steric contacts between host and guest, as they are avoided due to the almost free rotation ability of the benzene fragments. Actually, it is often observed in these nanohoops that the benzene rings adopt an alternating conformation (each benzene moiety is slightly inclined with respect to the neighboring rings) minimizing in this way destabilizing contacts. In order to illustrate the spatial region in which noncovalent interactions appear, an isosurface of 0.4 a.u. value is chosen to plot the RDG. Interestingly, this three dimensional representation produces a clear *interaction belt* between DQ and the CPP host (Figure 2B).

When performing this kind of analysis for all the DQ@CPP complexes, the effect of the empty space in the cavity can be clearly observed: the larger the empty space, the lower the density of noncovalent interactions. However, if the cavity is too tight (as in [7] and [8]-CPP), some repulsive interactions start to arise. In Figure 3, a color scale between −0.030 a.u.

DOI: 10.1021/acsomega.8b02673
ACS Omega 2018, 3, 16976−16988

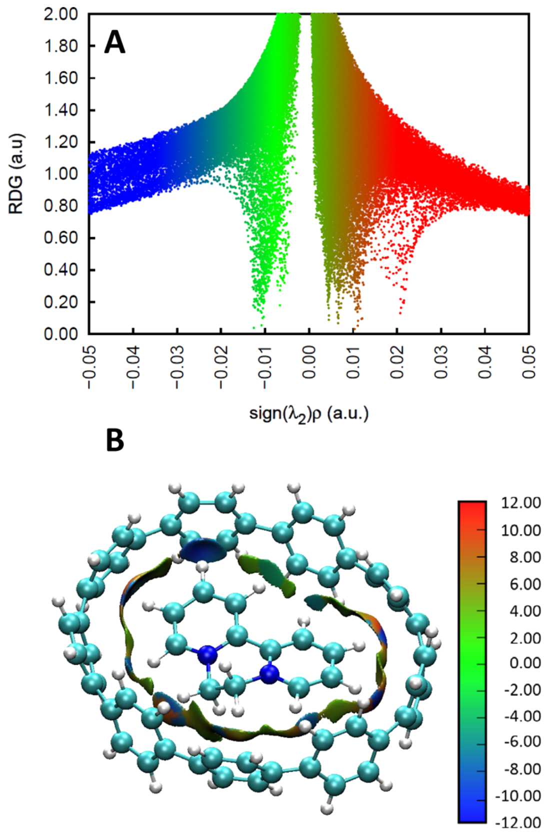

Figure 2. (A) Scatter graph of the RDG vs the sign of the second eigenvalue of the Hessian matrix multiplied by the electron density. (B) Spatial visualization of noncovalent interactions in the [9]-CPP system using a 0.4 a.u. isosurface. A color scale (in a.u.) is used to differentiate strong (blue) from weak attractive interactions (green) and from repulsive ones (red). Intramolecular repulsive noncovalent interactions at the center of the benzene rings have been removed for clarity.

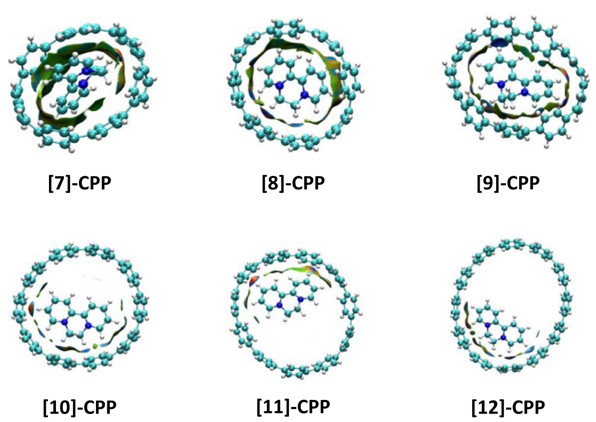

Figure 3. Spatial regions where noncovalent interactions occur in [7] to [12]-CPP systems as revealed by the NCI method (0.4 a.u. isosurface). The color scale is the same shown in subfigure B at Figure 2.

(dark blue) and +0.025 a.u. (red) has been chosen in order to represent NCI interactions in the DQ@CPP complexes, so that interaction regions of stabilizing and destabilizing nature can be differentiated. In the case of [7]-CPP, the large size of the isosurface indicates the existence of numerous interactions; however, the green tone of most of them indicates their weak (both stabilizing and destabilizing) character. Close contacts between C−H groups and the center of the benzene ring are established and repulsive interaction domains appear in these regions, even if their magnitude is not high. [8]-CPP also displays an extended RDG surface but the weak interaction regions (green) are less dominant and are replaced by stronger and attractive interaction regions (blue), as is also reflected in the interaction energy values collected in Table 1. Larger rings ([10] to [12]-CPP) show less effective interacting isosurfaces as the cavity is too big for DQ. [9]-CPP is a sweet spot where the fit with DQ is close enough to maximize the interacting surface but the cavity is also spacious enough to avoid repulsive steric contacts as shown on Figure 3. Actually, the presence of several blue domains in the interacting belt of [9]-CPP highlights medium-to-high energy stabilizing contacts (some repulsive CH-benzene ring contacts are still present as well).

In view of these reduced gradient isosurfaces and the energies collected in Table 1, it seems reasonable to propose [9]-CPP as the best structure for capturing DQ because of the existence of the right balance between the deformation necessary to obtain a complex with close stabilizing contacts and the resulting favorable interactions.

As has been explained in the Computational Methods section, SAPT allows us to dissect the interaction energy as a combination of four terms with clear physical meaning: electrostatic, exchange, induction, and dispersion energies. In this work, we use the SAPT0 a truncation of the perturbation to second order based on HF wavefunctions. Recently, a powerful methodology has been developed to further decompose these four energy terms into molecular fragment contributions. This is especially interesting to understand how each chemical group contributes to the global interaction energy and can be the basis of a campaign of rational design of hosts. Therefore, the four terms in which the interaction energy is decomposed, have also been dissected according to different molecular fragments with the reduced F-ISAPT0 method.[58−61] In this method, we have assumed that when cleaving a covalent bond to define the chemical groups its contribution is split 50:50 to each fragment. DQ is considered always as a single entity, while the [*n*]-CPP moiety is fragmented into phenylene groups.

Results from the SAPT0 dissection of the interaction energy between the DQ and the different [*n*]-CPP considered are summarized in Table 2. All complexes are dominated by stabilizing components (electrostatic, induction, and dispersion), among which the electrostatic contribution is quite high (around 30%) because we are dealing with charged systems. Induction terms are also significant (around 30% as well). The overall induction term can be decomposed in two parts: the induction of CPP due to the presence of DQ and vice versa. The global induction value is clearly dominated by the $Ind_{DQ\rightarrow CPP}$ term because of the polarizing ability of the cationic pesticide inside the nanohoop.

The dispersion contribution shows an interesting trend when considering the ring size. For *tight* cavities, where NCI analysis displayed a full *interaction belt*, the dispersion energy is strongly stabilizing (around −200 kJ/mol), whereas systems with broad cavities and looser bonding feature less stabilizing dispersive interactions (around −130 kJ/mol). There is therefore a clear energy gap between the values found for CPP[7]-CPP[9] and those corresponding to larger nanorings. These larger values in smaller rings are due to the numerous stacking and CH−π interactions present in these complexes.

DOI: 10.1021/acsomega.8b02673
ACS Omega 2018, 3, 16976−16988

Table 2. Interaction Energy Components Obtained after Decomposition with the SAPT0 Method and Jun-cc-pVDZ Basis Set for [7]-CPP to [12]-CPP[a]

N	electrostatic	exchange	$Ind_{CPP\to DQ}$	$Ind_{DQ\to CPP}$	Ind_{Total}	dispersion	total
7	−103.36	193.00	−2.70	−131.23	−133.93	−210.39	−254.69
8	−159.03	270.01	−2.09	−160.57	−162.65	−226.67	−278.34
9	−169.21	235.41	−1.30	−171.41	−172.71	−206.72	−313.23
10	−131.72	150.72	−0.97	−139.64	−140.61	−143.54	−265.15
11	−116.17	135.82	−0.97	−117.99	−118.96	−128.73	−228.06
12	−123.30	150.90	−1.05	−135.70	−136.75	−133.83	−242.99

[a]All energies are given in kJ/mol.

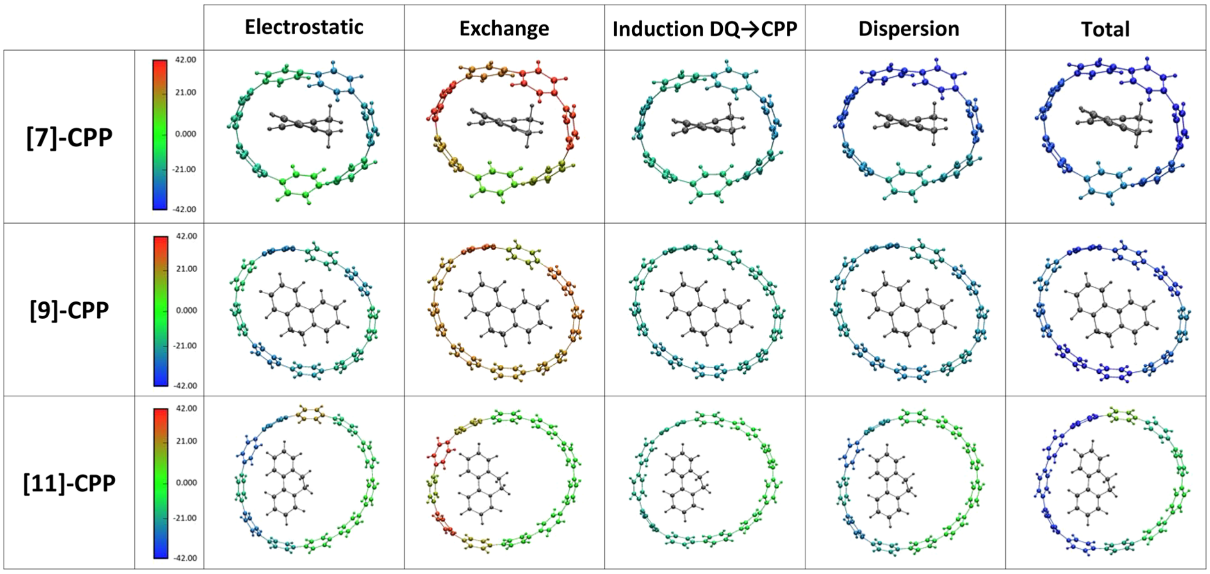

Figure 4. Different contributions to the interaction energy decomposed using the F-ISAPT methodology for selected systems. The supramolecular complex is divided into the DQ moiety and each of the benzene rings of the nanohoop as fragments. A color scale ranging from −42.0 kJ/mol (blue) to 42.0 kJ/mol (red) is used to help visualize the interactions of each fragment.

The exchange energy term follows a trend similar to dispersion because both depend on the number of C−C, C−N and C−H contacts at short distances.

According to all the contributions shown in Table 2, [9]-CPP benefits from a relatively low exchange + dispersion penalty when compared to other systems with *tight* and strongly interacting cavities and very favorable electrostatic and induction terms. [7]-CPP and [8]-CPP show slightly more favorable dispersion interactions, but at the cost of poorer induction or electrostatic stabilization. Moreover, [8]-CPP pays a fortune in terms of exchange repulsion which cannot be compensated by the slightly better vdW interactions.

As mentioned above, perhaps the most interesting part of the decomposition of interaction energies is to be able to attribute a certain amount of each of the energetic components to the different molecular groups of the systems studied. A detailed analysis on the nanoring fragment contributions to these energy terms is illustrated in Figure 4. We have performed this analysis for three representative complexes: the most stable ([9]-CPP), the smallest ([7]-CPP), and one of the largest rings ([11]-CPP), all of them with an odd number of benzene moieties in the nanohoop.

For the most stable one ([9]-CPP), a dark blue tone (values of −26.4 and −22.12 kJ/mol) is observed in the electrostatic component in the two rings closest to the nitrogen atoms of the DQ moiety, it corresponds to the strong electrostatic cation−π interactions between the most positively charged region of DQ and the two closest benzene rings of the CPP. There are also two other phenylene fragments that display a very significant contribution to the global electrostatics of the system (−25.9 and −23.4 kJ/mol respectively). These interactions are due to the C−H−π contacts with the hydrogen atoms in para position with respect to the N atoms in DQ. Both the N atoms and the C−H groups in para feature significant positive partial charge, hence the high electrostatic component. However, this also produces geometric proximity with the phenylene fragments of the nanoring and, as a consequence, exchange repulsion. Interestingly, the attractive electrostatic component and the exchange repulsion almost cancel out for both kinds of fragments (N atoms and the C−H in para), which implies that the eventual complex stability can be diagnosed in terms of induction and dispersion terms only. The $Ind_{DQ\to CPP}$ induction and dispersion terms display a more homogeneous character. They are stabilizing all along the perimeter of [9]-CPP in about −19 and −23 kJ/mol per phenylene fragment for induction and dispersion, respectively, but the two rings interacting with the N atoms show significantly higher values (−22.6 and −25.2 kJ/mol). In the case of induction, these larger values can be assigned again to the localized charge on the N atoms, which exert a strong polarizing effect.

In the larger system (11-[CPP]), there is a large unused volume of the cavity so, to maximize the DQ−CPP interactions, the guest is displaced to one side of the

DOI: 10.1021/acsomega.8b02673
ACS Omega 2018, 3, 16976−16988

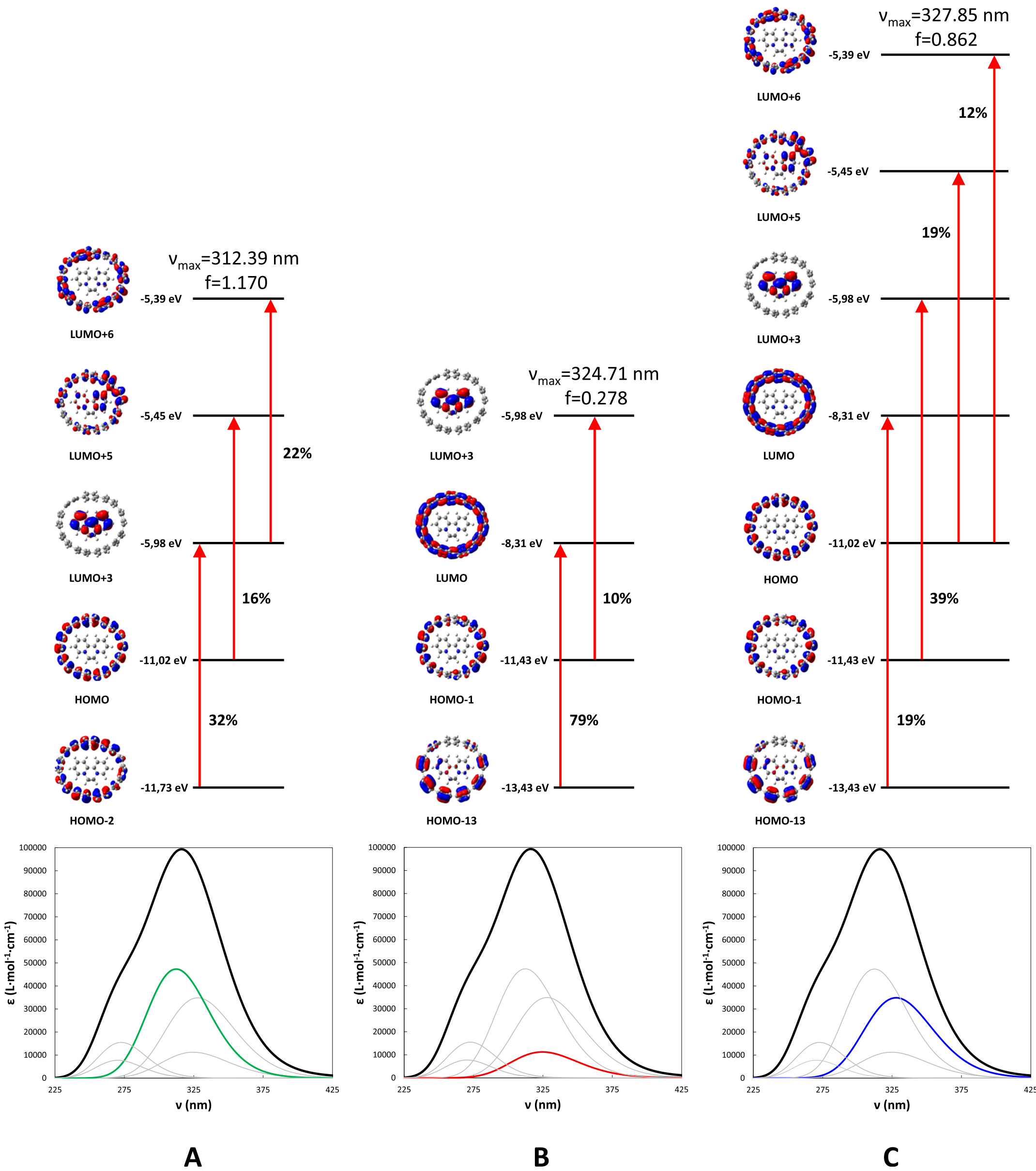

Figure 5. Main electronic transitions that contribute to the maximum in the UV−vis spectrum of DQ@[9]-CPP. Each of these transitions (colored in green, red, and blue) are composed of various transits between orbitals (orbital energy is given in eV). The percentage values show the contribution of each transit to the global band. The remaining amount up to 100% comes from various transits with minor weights. For each of the marked bands, the position of the maximum (in nm) and the oscillator strength associated with the electronic transition is provided. The molecular orbitals are represented with a 0.02 isovalue displaying positive values in red and negative in blue.

nanohoop, deforming the ring in that direction. This effect can be easily appreciated using the F-ISAPT0 analysis. The electrostatic component is clearly more favorable in the rings having direct interaction with the DQ and practically negligible in the most remote phenylene moieties. In the [11]-CPP complex, there are two cases where the benzene rings have a positive (repulsive) electrostatic component. The benzene moiety marked in light brown in the electrostatic component destabilizes the global system by 23.90 kJ/mol, a large contribution that can hardly be compensated with other favorable contributions. Actually, that phenylene fragment alone displays a global contribution of +12.79 kJ/mol, that is, it destabilizes the complex. Four phenylene rings further away in DQ, we find another ring with a positive electrostatic component but much less intense (1.10 kJ/mol). In this ring, the stabilizing energy components are also small thus making for an almost irrelevant global contribution to the complexation energy of this fragment (−1.68 kJ/mol). The major contributions of DQ → CPP induction and highly stabilizing dispersion components occur in the rings closest to DQ. Unlike [9]-CPP in which the contributions of the electrostatics and the exchange were almost compensated, in this case, the sum of both yields stabilizing results due to the greater magnitude of the electrostatics.

In [7]-CPP, a slightly different situation can be found as the small size of the cavity causes the DQ guest to adopt a different orientation, perpendicular to the nanohoop with the strongly positive zones associated to the N atoms poised very close to some phenylene rings. It is worth mentioning that DQ is slightly displaced from the center of the nanohoop toward one of the sides of the cavity. This fact and the conformation of the phenylene fragments results, despite the high degree of

DOI: 10.1021/acsomega.8b02673
ACS Omega 2018, 3, 16976−16988

confinement of the guest inside of the cavity, in a differentiated behavior between fragments. As shown in Figure 4, even with such a tight cavity, one phenylene unit hardly contributes to the electrostatics of the exchange energies (in bright green color). However, the non-negligible induction and dispersion terms entail that the contribution of this ring to the global interaction energy is about 10% of the total stability. The greatest electrostatic interaction occurs between the positive region of DQ (including here the N atoms and aliphatic bridge that joins them) with the closest benzene rings. These phenylene fragments are therefore the ones that contribute the most to global energy (19.0 and 16.4% respectively). These two significant contributions are reinforced by having the greatest dispersion contributions. The DQ → CPP induction term is in this case quite similar in all fragments, with an average value of −18.75 kJ/mol. As in all the analyzed systems, the reverse CPP → DQ induction does not play any relevant role for the global energy (it contributes only 1% to the global of [7]-CPP, 0.4% in [9]-CPP and 0.43% in the [11]-CPP system).

3.1. Exploring the Sensing Ability of [9]-CPP System: RR Spectroscopy. Prior to capturing the pesticide, its detection in complex matrices like plants or substrate is needed. The high binding energies to [*n*]-CPPs found for DQ make attractive the possibility of using these complexes as sensing devices. In order to explore this potential, we performed simulations of Raman spectra. The reasoning behind this choice of technique are the advantages that vibrational spectroscopy provides for the study of nanohoops and the fact that the pesticide is a good chromophore. Making use of Raman spectroscopy, Chen et al. have already determined that [*n*]-CPPs possess characteristic vibrations that converge with those exhibited by long polyparaphenylenes as their size increases.[70,71] These size-dependent Raman modes were studied experimentally and confirmed by means of quantum chemical calculations. We propose the use of RR spectroscopy because it leads to larger intensities and likely better detection limits than other vibrational spectroscopies. As far as we know, although Raman and vibrational resonance techniques are widely used in nanotubes due to their nondestructive nature and the ability to probe both elastic and electronic structures,[72−78] until now RR spectroscopy has never been applied to [*n*]-CPPs.

Prior to the computation of the RR spectra, we simulated the UV−vis absorption ones, which helped us choose the transitions with larger oscillator strengths. The electronic absorption spectrum of the DQ@[9]-CPP system (Figure 5) spans 200 nm between 225 and 425 nm forming a wide band with a maximum at 316 nm and a shoulder located at around 265 nm. As it can be seen in Figure 5, at the maximum of the band three transitions contribute significantly. The one shown in green has the maximum placed at ν_{max} = 312.4 nm with an oscillator strength of 1.170 (with a global contribution of 31.1%). The maximum of the one shown in red is placed at 324.7 nm (f = 0.278, contribution 10.6%), while the one marked in blue is about 3 nm away from the previous one, ν_{max} = 327.9 nm (f = 0.862, contribution 46.9%). These are complex transitions which are composed of several transits between molecular orbitals, as indicated in Figure 5.

RR usually provides optimum response near the UV−vis absorption maxima, but there is no rule of thumb to decide in which direction and what step size to walk away from the exact maximum. Additionally, the UV−vis simulations of the complex produced an absorption band bracketed between 225 and 425 nm (see Figure 5) but the UV−vis spectrum of isolated DQ ranges between 100 and 350 nm (see Supporting Information). We have therefore carried out a systematic study to calculate the RR spectra employing incident wavelengths in 100−350 nm range of the UV spectrum by sampling every 2 nm, hence including the complex maximum and the isolated pesticide signal. The global composition of the individual spectra generates the three-dimensional amplified spectrum shown in Figure 6.

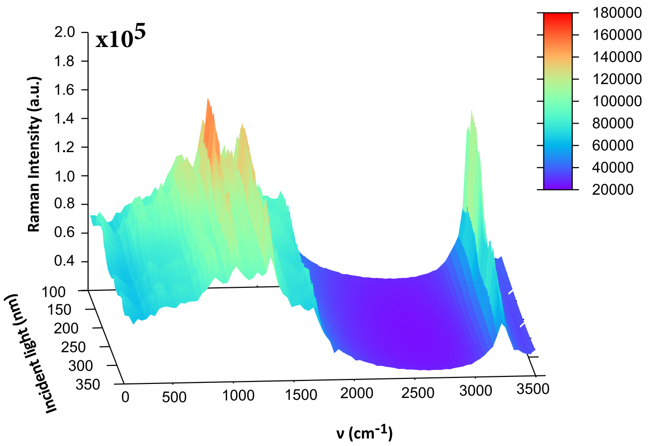

Figure 6. Three-dimensional RR spectrum showing the Raman intensity (a.u.) of each of the vibrational modes in the range between 0 and 3500 cm^{-1} as a function of the laser incident wavelength (in nm). To facilitate the visualization a color scale between violet (low intensity) and red (high intensity) has been used.

To select the optimum wavelengths from the 3D RR spectrum shown in Figure 6 to be used as incident lights, a double criterion must be used: one based on the signal/noise ratio and the other one based on selecting vibrations that allow a selective identification of the guest molecule. In the first place, in terms of the signal-to-noise ratio, it is important that the vibrations appear well defined in the spectrum, with not many contiguous bands, in order to facilitate identification. Secondly, to carry out a selective identification, it is convenient that the chosen vibrations are characteristic of the particular molecule under study, in this case DQ. For this purpose, through the visualization of the vibrational modes and their comparison with the vibrations of isolated DQ, 10 characteristic vibrations with potential to be used as diagnostic signals have been selected (see Table 3). These vibrations include stretching (ν) of the CH groups that join both pyridine rings of the DQ moiety located at 3190.2 and 3193.6 cm^{-1}, stretching (ν) of the rings of the DQ (1665.9 cm^{-1}), CH_2 wagging (ω) (1259.4 cm^{-1}), out-of-plane deformation (γ) of DQ rings (743.5 cm^{-1}), in-plane bending (δ), and out-of-plane bending (γ) of the CH groups (1442.2 and 943.6 cm^{-1} respectively) as well as other combined vibrational modes at 1530.1, 1319.0, and 1098.7 cm^{-1}. In all cases, the vibrational modes of DQ complexed inside of [9]-CPP experience displacements with respect to isolated DQ between 0.5 and 13.87 cm^{-1}, which allows us to discern if the DQ is inside of [9]-CPP or not. Only two of these modes (1319.0 and 1442.2 cm^{-1}) are slightly coupled with vibrations of the cyclo-paraphenylene structure.

DOI: 10.1021/acsomega.8b02673
ACS Omega 2018, 3, 16976−16988

Table 3. Vibrational Modes Selected To Identify DQ Inside the [9]-CPP System[a]

frequency	static limit	272 nm	322 nm	326 nm	DQ	assignement
743.45	26.88		2.11×10^5 (3.90)		742.95	$\gamma_{skeleton}$
943.62	3.40		1.67×10^6 (5.69)	5.36×10^6 (6.20)	935.48	γ_{CH}
1098.71	45.11	1.19×10^6 (4.42)	2.13×10^6 (4.67)		1099.5	$\delta_{ring} + \delta_{CH}$
1259.43	15.11	2.79×10^5 (4.27)	1.03×10^6 (4.83)	4.21×10^6 (5.44)	1263.51	ω_{CH_2}
1319.04	11.92		3.78×10^5 (4.50)	7.18×10^4 (3.78)	1327.96	$\nu_{CH} + \delta_{CH} + \omega_{CH_2}$
1442.21	10.65	5.05×10^6 (5.68)	9.65×10^6 (5.96)		1452.73	δ_{CH}
1530.13	0.79	8.61×10^6 (7.04)	2.20×10^6 (6.45)		1536.36	$\nu_{ring} + \delta_{CH}$
1665.88	7.14		4.55×10^5 (4.80)	3.50×10^6 (5.69)	1666.87	ν_{ring}
3176.31	41.86		7.95×10^7 (6.28)		3190.18	ν_{CH}
3182.62	36.38	8.95×10^5 (4.39)	7.30×10^6 (5.30)		3193.62	ν_{CH}

[a]The frequency of all the vibrations is given in cm^{-1}. The static limit shows the intensity of the conventional Raman spectrum in which no incident light wavelength has been used. Amplified Raman intensities (in arbitrary units) are given for incident light frequency 272, 322, and 326 nm. Parentheses show the enhancement factor, defined as the logarithm of the quotient between the amplified intensity and the corresponding intensity of the static limit. The location of the corresponding isolated DQ vibrations mode is also given. Finally, the assignment of the selected vibrational modes is shown where ν corresponds to stretching modes, δ with in-plane bending vibrations, γ are out-of-plane vibrations, and ω refers to wagging molecular displacements. Note that no scaling factors were used for these frequencies.

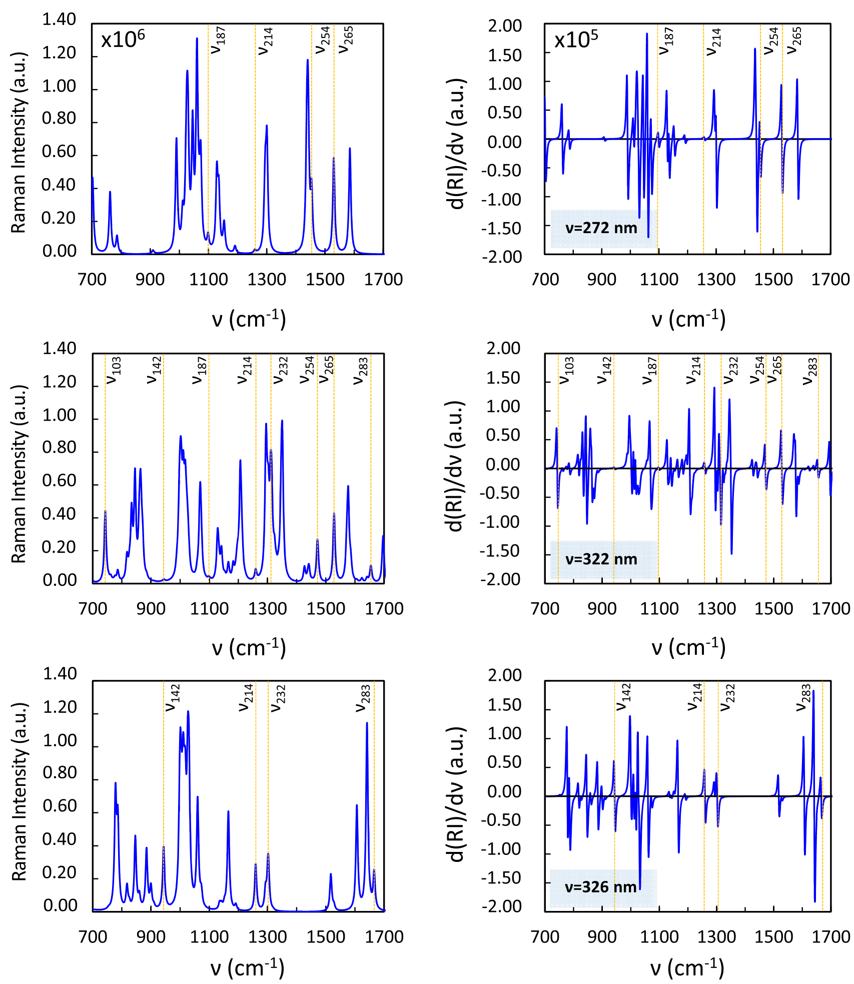

Figure 7. Raman intensity spectra for the DQ-[9]-CPP system considering three different incident laser wavelengths (272, 322, and 326 nm) are shown on the left. The corresponding derivative RR spectra are represented on the right. Incident wavelengths represented are 272 nm (top), 322 nm (middle), and 326 nm (bottom). Raman intensities for the original spectra are shown scaled with a factor of 10^6, while their first derivatives are scaled by 10^5. Indexes correspond to Table 3.

According to the selection criteria mentioned above, three wavelengths have been chosen as candidates for sensing purposes: 272, 322, and 326 nm. Interestingly, they correspond with slight displacements (around 2−3 nm) from relevant points in the UV−vis spectrum previously computed. The 272 nm value is close to the electronic transitions that give rise to the shoulder in this spectrum, while the other two are placed close to the absorption maximum. Figure 7 shows the

DOI: 10.1021/acsomega.8b02673
ACS Omega 2018, 3, 16976−16988

amplified and indexed Raman spectra for the three selected incident wavelengths as well as their first derivative. The use of derived spectroscopy facilitates the study of bands that are mixed (overlapped) or very close to each other, hence helping distinguish isolated from complexed DQ scenarios. It should be mentioned that due to the orbitals that participate in each of the transitions, not all the vibrations are amplified when using incident light of the selected wavelengths. In Table 3, the enhancement factor for each of the vibrational modes has been included in parentheses, a parameter that accounts for the magnitude of the amplification with respect to the value of Raman intensity in the static limit. Although some of the bands indicated in the spectrum may seem of very low intensity, they are perfectly valid for sensing applications with nanohoops because the Raman intensity is multiplied by a factor of 10^6 in the RR spectra and 10^5 in the first derivative resonant Raman spectroscopy. On the basis of the data shown, any of the incident wavelengths selected would be a good candidate for a sensing study; however, 322 nm can be regarded as the most promising one because of the number of amplified vibrational modes and high enhancement factors.

4. CONCLUSIONS

- Novel [*n*]-CPP architectures can be used for the capture of the DQ pesticide. A size-dependent complexation study was done showing that [9]-CPP is the most suitable nanohoop for complexation of this molecule.
- Complexation energies as high as −257.6 kJ/mol are obtained for the optimum size system, although there is an energy penalty (between 9.2 and 32.6 kJ/mol) to overcome because of the deformation of fragments with respect to their isolated geometries.
- To maximize interactions with the DQ pesticide in bigger cycloparaphenylenes, the molecule is displaced to one side and highly deforms the ring. Because of the high flexibility of the hoop, there is not a big energy penalty associated to this process. However, lower interaction energies are obtained because of the existence of a large void space that does not allow short-range interactions to stabilize half of the guest.
- Complexes are dispersion dominated and also have high DQ→CPP induction contributions. In the optimum [9]-CPP, each energy contribution to the total interaction energy is well balanced between all the rings, while in bigger ones there are clear local high contributions where the DQ is placed and almost negligible in the most remote ones.
- The use of RR spectroscopy allows us to perform DQ sensing by rational selection of the incident laser wavelengths. 322 nm was shown to be the best option for the study of the DQ-[9]-CPP system because of the good signal-to-noise ratio and the number of vibrational modes that allow selective identification.
- Significant vibrations of DQ show a displacement with respect to isolated gas phase calculations, which allows us to discern if the complexation was achieved or not. The use of first derivative spectroscopy makes it easier to identify the position of characteristic vibrations, especially in cases where they are close to other bands.

These results suggest that CPPs could be a promising approach for DQ encapsulation and sensing, allowing the formation of remarkably stable complexes and providing a set of characteristic vibrations which could be used as DQ tracers.

■ ASSOCIATED CONTENT

Supporting Information

The Supporting Information is available free of charge on the ACS Publications website at DOI: 10.1021/acsomega.8b02673.

Detailed F-ISAPT0 contributions, calculations on solvation effects, and an estimation of the barrier for the complexation process in [9]-CPP (PDF)

■ AUTHOR INFORMATION

Corresponding Authors

*E-mail: carlos.silva@uvigo.es (C.S.L.).

*E-mail: faza@uvigo.es (O.N.F.).

ORCID

Ángel Vidal-Vidal: 0000-0002-5876-5431

Enrique M. Cabaleiro-Lago: 0000-0001-5848-6523

Carlos Silva López: 0000-0003-4955-9844

Olalla Nieto Faza: 0000-0001-8754-1341

Notes

The authors declare no competing financial interest.

■ ACKNOWLEDGMENTS

The authors thank the Centro de Supercomputación de Galicia (CESGA) for the generous allocation of computer time. Ministerio de Economía y Competitividad (MINECO, PCTQ2016-75023-C2-2-P) and Consellería de Cultura, Educación e Ordenación Universitaria e da Consellería de Economía, Emprego e Industria (Axuda para Consolidación e Estruturación de unidades de investigación competitivas do Sistema Universitario de Galicia, Xunta de Galicia ED431C 2017/17) are also acknowledged. Á.V.V. is grateful to the Universidade de Vigo for a predoctoral fellowship.

■ REFERENCES

(1) Cooper, J.; Dobson, H. The Benefits of Pesticides to Mankind and the Environment. *Crop Prot.* **2007**, *26*, 1337−1348.

(2) Ecobichon, D. J. Our changing perspectives on benefits and risks of pesticides: a historical overview. *Neurotoxicology* **2000**, *21*, 211−218.

(3) Abdollahzadeh, G.; Sharifzadeh, M. S.; Damalas, C. A. Perceptions of the Beneficial and Harmful Effects of Pesticides Among Iranian Rice Farmers Influence the Adoption of Biological Control. *Crop Prot.* **2015**, *75*, 124−131.

(4) Tyler Miller, G.; Spoolman, S. *Sustaining the Earth*, 10th ed.; Brooks Cole, 2011.

(5) Lewis, K. A.; Tzilivakis, J.; Warner, D. J.; Green, A. An International Database for Pesticide Risk Assessments and Management. *Hum. Ecol. Risk Assess.* **2016**, *22*, 1050−1064.

(6) Stenersen, J. *Chemical Pesticides Mode of Action and Toxicology*; CRC Press, 2004.

(7) Waxman, M. F. *The Agrochemical and Pesticides Safety Handbook*; CRC Press, 1998.

(8) Pateiro-Moure, M.; Arias-Estévez, M.; Simal-Gándara, J. Critical Review on the Environmental Fate of Quaternary Ammonium Herbicides in Soils Devoted to Vineyards. *Environ. Sci. Technol.* **2013**, *47*, 4984−4998.

(9) Pomeroy, A. *Biochemical Mechanisms of Paraquat Toxicity*; Academic Press, 1977.

(10) FAO; WHO. *Pesticide Residues in Food 2004. FAO Panel of Experts on Pesticide Residues in Food and the Environment and the WHO Core Assessment Group*; FAO and WHO, 2004.

DOI: 10.1021/acsomega.8b02673
ACS Omega 2018, 3, 16976−16988

(11) Yamamoto, I.; Katsuda, Y. β-cyclodextrin inclusion complexes of pyrethroids. *Pestic. Sci.* **1980**, *11*, 134−140.
(12) Luo, L.; Zhang, X.; Feng, N.; Tian, D.; Deng, H.; Li, H. Cation-Induced Pesticide Binding and Release by a Functionalized Calix[4]-arene Molecular Host. *Sci. Rep.* **2015**, *5*, 8982.
(13) Flaherty, R. J.; Nshime, B.; DeLaMarre, M.; DeJong, S.; Scott, P.; Lantz, A. W. Cyclodextrins as Complexation and Extraction Agents for Pesticides From Contaminated Soil. *Chemosphere* **2013**, *91*, 912−920.
(14) Zhang, X.; Liu, J.; Hou, W.; Tong, J.; Ren, L.; Sun, G.; Sun, Y. Preparation and Properties of Pesticide/Cyclodextrin Complex Intercalated into ZnAl-Layered Double Hydroxide. *Ind. Eng. Chem. Res.* **2016**, *55*, 1550−1558.
(15) Szejtli, J. Cyclodextrins in Pesticides. *Starch Staerke* **1985**, *37*, 382−386.
(16) Li, P.-Z.; Su, J.; Liang, J.; Liu, J.; Zhang, Y.; Chen, H.; Zhao, Y. A Highly Porous Metal-Organic Framework for Large Organic Molecule Capture and Chromatographic Separation. *Chem. Commun.* **2017**, *53*, 3434−3437.
(17) Chen, D.-M.; Tian, J.-Y.; Wang, Z.-W.; Liu, C.-S.; Chen, M.; Du, M. An Anionic Na(i)-Organic Framework Platform: Separation of Organic Dyes and Post-Modification for Highly Sensitive Detection of Picric Acid. *Chem. Commun.* **2017**, *53*, 10668−10671.
(18) Ferreira, L. V.; Machado, I.-F. Surface Photochemistry: Organic Molecules within Nanocavities of Calixarenes. *Curr. Drug Discovery Technol.* **2007**, *4*, 229−245.
(19) Nabok, A. V.; Hassan, A. K.; Ray, A. K.; Omar, O.; Kalchenko, V. I. Study of Adsorption of Some Organic Molecules in Calix[4]resorcinolarene LB Films by Surface Plasmon Resonance. *Sens. Actuators, B* **1997**, *45*, 115−121.
(20) Macartney, D. H. Encapsulation of Drug Molecules by Cucurbiturils: Effects on their Chemical Properties in Aqueous Solution. *Isr. J. Chem.* **2011**, *51*, 600−615.
(21) Robinson-Duggon, J.; Pérez-Mora, F.; Dibona-Villanueva, L.; Fuentealba, D. Potential Applications of Cucurbit[n]urils Inclusion Complexes in Photodynamic Therapy. *Isr. J. Chem.* **2017**, *58*, 199−214.
(22) Sleziakova, K.; Avei, M. R.; Kaifer, A. E.; Sindelar, V. Binding of bambusuril with bipyridinium guests in water. *Supramol. Chem.* **2017**, *10*, 832−837.
(23) Fan, H.; Gu, J.; Meng, H.; Knebel, A.; Caro, J. High-Flux Membranes Based on the Covalent Organic Framework COF-LZU1 for Selective Dye Separation by Nanofiltration. *Angew. Chem., Int. Ed.* **2018**, *57*, 4083−4087.
(24) Jasti, R.; Bhattacharjee, J.; Neaton, J. B.; Bertozzi, C. R. Synthesis, Characterization, and Theory of [9]-, [12]-, and [18]-Cycloparaphenylene: Carbon Nanohoop Structures. *J. Am. Chem. Soc.* **2008**, *130*, 17646−17647.
(25) Segawa, Y.; Miyamoto, S.; Omachi, H.; Matsuura, S.; Šenel, P.; Sasamori, T.; Tokitoh, N.; Itami, K. Concise Synthesis and Crystal Structure of [12]Cycloparaphenylene. *Angew. Chem., Int. Ed.* **2011**, *50*, 3244−3248.
(26) Xia, J.; Jasti, R. Synthesis, Characterization, and Crystal Structure of [6]Cycloparaphenylene. *Angew. Chem., Int. Ed.* **2012**, *51*, 2474−2476.
(27) Segawa, Y.; Senel, P.; Matsuura, S.; Omachi, H.; Itami, K. 9-Cycloparaphenylene: Nickel-mediated Synthesis and Crystal Structure. *Chem. Lett.* **2011**, *40*, 423−425.
(28) Kayahara, E.; Sakamoto, Y.; Suzuki, T.; Yamago, S. Selective Synthesis and Crystal Structure of [10]Cycloparaphenylene. *Org. Lett.* **2012**, *14*, 3284−3287.
(29) Darzi, E. R.; Jasti, R. The dynamic, size-dependent properties of [5]-[12]cycloparaphenylenes. *Chem. Soc. Rev.* **2015**, *44*, 6401−6410.
(30) Golder, M. R.; Jasti, R. Syntheses of the Smallest Carbon Nanohoops and the Emergence of Unique Physical Phenomena. *Acc. Chem. Res.* **2015**, *48*, 557−566.
(31) Van Raden, J. M.; Louie, S.; Zakharov, L. N.; Jasti, R. 2,2′-Bipyridyl-Embedded Cycloparaphenylenes as a General Strategy To Investigate Nanohoop-Based Coordination Complexes. *J. Am. Chem. Soc.* **2017**, *139*, 2936−2939.
(32) Segawa, Y.; Fukazawa, A.; Matsuura, S.; Omachi, H.; Yamaguchi, S.; Irle, S.; Itami, K. Combined Experimental and Theoretical Studies on the Photophysical Properties of Cycloparaphenylenes. *Org. Biomol. Chem.* **2012**, *10*, 5979−5984.
(33) Iwamoto, T.; Watanabe, Y.; Sakamoto, Y.; Suzuki, T.; Yamago, S. Selective and Random Syntheses of [n]Cycloparaphenylenes (n= 8-13) and Size Dependence of Their Electronic Properties. *J. Am. Chem. Soc.* **2011**, *133*, 8354−8361.
(34) Kayahara, E.; Fukayama, K.; Nishinaga, T.; Yamago, S. Size Dependence of [n]Cycloparaphenylenes (n=5-12) in Electrochemical Oxidation. *Chem.−Asian J.* **2016**, *11*, 1793−1797.
(35) Darzi, E. R.; Jasti, R. The Dynamic, Size-Dependent Properties of [5]-[12]cycloparaphenylenes. *Chem. Soc. Rev.* **2015**, *44*, 6401−6410.
(36) Ball, M.; Nuckolls, C. Stepping into the Light: Conjugated Macrocycles with Donor-Acceptor Motifs. *ACS Cent. Sci.* **2015**, *1*, 416−417.
(37) Ball, M.; Zhong, Y.; Fowler, B.; Zhang, B.; Li, P.; Etkin, G.; Paley, D. W.; Decatur, J.; Dalsania, A. K.; Li, H.; Xiao, S.; Ng, F.; Steigerwald, M. L.; Nuckolls, C. Macrocyclization in the Design of Organic n-Type Electronic Materials. *J. Am. Chem. Soc.* **2016**, *138*, 12861−12867.
(38) Neuhaus, P.; Cnossen, A.; Gong, J. Q.; Herz, L. M.; Anderson, H. L. A Molecular Nanotube with Three-Dimensional π-Conjugation. *Angew. Chem., Int. Ed.* **2015**, *54*, 7344−7348.
(39) Iwamoto, T.; Slanina, Z.; Mizorogi, N.; Guo, J.; Akasaka, T.; Nagase, S.; Takaya, H.; Yasuda, N.; Kato, T.; Yamago, S. Partial Charge Transfer in the Shortest Possible Metallofullerene Peapod, La@C82⊂[11]Cycloparaphenylene. *Chem.—Eur. J.* **2014**, *20*, 14403−14409.
(40) Ueno, H.; Nishihara, T.; Segawa, Y.; Itami, K. Cycloparaphenylene-Based Ionic Donor-Acceptor Supramolecule: Isolation and Characterization of Li+@C60⊂[10]CPP. *Angew. Chem., Int. Ed.* **2015**, *54*, 3707−3711.
(41) Xia, J.; Bacon, J. W.; Jasti, R. Gram-scale synthesis and crystal structures of [8]- and [10]CPP, and the solid-state structure of C60@[10]CPP. *Chem. Sci.* **2012**, *3*, 3018−3021.
(42) Iwamoto, T.; Watanabe, Y.; Sadahiro, T.; Haino, T.; Yamago, S. Size-Selective Encapsulation of C60 by [10]Cycloparaphenylene: Formation of the Shortest Fullerene-Peapod. *Angew. Chem., Int. Ed.* **2011**, *50*, 8342−8344.
(43) Vidal Vidal, Á.; López, C. S.; Nieto Faza, O. Nitrogen Doped Nanohoops as Promising CO2 Capturing Devices. *Phys. Chem. Chem. Phys.* **2018**, *20*, 8607−8615.
(44) Josa, D.; González-Veloso, I.; Rodríguez-Otero, J.; Cabaleiro-Lago, E. M. Tailoring Buckybowls for Fullerene Recognition. a Dispersion-Corrected DFT Study. *Phys. Chem. Chem. Phys.* **2015**, *17*, 6233−6241.
(45) González-Veloso, I.; Rodríguez-Otero, J.; Cabaleiro-Lago, E. M. Carbon-Nanorings ([10]CPP and [6]CPPA) as Fullerene (C60 and C70) Receptors: A Comprehensive Dispersion-Corrected DFT Study. *Phys. Chem. Chem. Phys.* **2016**, *18*, 31670−31679.
(46) Nakanishi, Y.; Omachi, H.; Matsuura, S.; Miyata, Y.; Kitaura, R.; Segawa, Y.; Itami, K.; Shinohara, H. Size-Selective Complexation and Extraction of Endohedral Metallofullerenes with Cycloparaphenylene. *Angew. Chem., Int. Ed.* **2014**, *126*, 3166−3170.
(47) Della Sala, P.; Talotta, C.; Caruso, T.; De Rosa, M.; Soriente, A.; Neri, P.; Gaeta, C. Tuning Cycloparaphenylene Host Properties by Chemical Modification. *J. Org. Chem.* **2017**, *82*, 9885−9889.
(48) Frisch, M. J.; et al. *Gaussian 09 Revision D.01*; Gaussian Inc.: Wallingford CT 2009.
(49) Kolaski, M.; Kumar, A.; Singh, N. J.; Kim, K. S. Differences in Structure, Energy, and Spectrum Between Neutral, Protonated, and Deprotonated Phenol Dimers: Comparison of Various Density Functionals With Ab Initio Theory. *Phys. Chem. Chem. Phys.* **2011**, *13*, 991−1001.

DOI: 10.1021/acsomega.8b02673
ACS Omega 2018, 3, 16976−16988

(50) Lee, H. M.; Youn, I. S.; Saleh, M.; Lee, J. W.; Kim, K. S. Interactions of CO2 with various functional molecules. *Phys. Chem. Chem. Phys.* **2015**, *17*, 10925−10933.
(51) Jensen, J. H. Predicting accurate absolute binding energies in aqueous solution: thermodynamic considerations for electronic structure methods. *Phys. Chem. Chem. Phys.* **2015**, *17*, 12441−12451.
(52) Cossi, M.; Barone, V.; Cammi, R.; Tomasi, J. Ab initio study of solvated molecules: a new implementation of the polarizable continuum model. *Chem. Phys. Lett.* **1996**, *255*, 327−335.
(53) Tomasi, J.; Mennucci, B.; Cammi, R. Quantum Mechanical Continuum Solvation Models. *Chem. Rev.* **2005**, *105*, 2999−3094.
(54) Jeziorski, B.; Moszynski, R.; Szalewicz, K. Perturbation Theory Approach to Intermolecular Potential Energy Surfaces of van der Waals Complexes. *Chem. Rev.* **1994**, *94*, 1887−1930.
(55) Parker, T. M.; Burns, L. A.; Parrish, R. M.; Ryno, A. G.; Sherrill, C. D. Levels of Symmetry Adapted Perturbation Theory (SAPT). I. Efficiency and Performance for Interaction Energies. *J. Chem. Phys.* **2014**, *140*, 094106.
(56) Moszynski, R.; Jeziorski, B.; Ratkiewicz, A.; Rybak, S. Many-body perturbation theory of electrostatic interactions between molecules: Comparison with full configuration interaction for four-electron dimers. *J. Chem. Phys.* **1993**, *99*, 8856−8869.
(57) Moszyński, R.; Cybulski, S. M.; Chalasinski, G. Many-Body Theory of Intermolecular Induction Interactions. *J. Chem. Phys.* **1994**, *100*, 4998−5010.
(58) Parrish, R. M.; Sherrill, C. D. Spatial Assignment of Symmetry Adapted Perturbation Theory Interaction Energy Components: The Atomic SAPT Partition. *J. Chem. Phys.* **2014**, *141*, 044115.
(59) Parrish, R. M.; Parker, T. M.; Sherrill, C. D. Chemical Assignment of Symmetry-Adapted Perturbation Theory Interaction Energy Components: The Functional-Group SAPT Partition. *J. Chem. Theory Comput.* **2014**, *10*, 4417−4431.
(60) Parrish, R. M.; Sherrill, C. D. Quantum-Mechanical Evaluation of π-π versus Substituent−π Interactions in π Stacking: Direct Evidence for the Wheeler-Houk Picture. *J. Am. Chem. Soc.* **2014**, *136*, 17386−17389.
(61) Parrish, R. M.; Gonthier, J. F.; Corminbœuf, C.; Sherrill, C. D. Communication: Practical intramolecular symmetry adapted perturbation theory via Hartree-Fock embedding. *J. Chem. Phys.* **2015**, *143*, 051103.
(62) Parrish, R. M.; et al. Psi4 1.1: An Open-Source Electronic Structure Program Emphasizing Automation, Advanced Libraries, and Interoperability. *J. Chem. Theory Comput.* **2017**, *13*, 3185−3197.
(63) Papajak, E.; Zheng, J.; Xu, X.; Leverentz, H. R.; Truhlar, D. G. Perspectives on Basis Sets Beautiful: Seasonal Plantings of Diffuse Basis Functions. *J. Chem. Theory Comput.* **2011**, *7*, 3027−3034.
(64) Dunning, T. H., Jr. Gaussian Basis Sets for Use in Correlated Molecular Calculations. I. the Atoms Boron Through Neon and Hydrogen. *J. Chem. Phys.* **1989**, *90*, 1007−1023.
(65) Lu, T.; Chen, F. Multiwfn: A Multifunctional Wavefunction Analyzer. *J. Comput. Chem.* **2011**, *33*, 580−592.
(66) Johnson, E. R.; Keinan, S.; Mori-Sánchez, P.; Contreras-García, J.; Cohen, A. J.; Yang, W. Revealing Noncovalent Interactions. *J. Am. Chem. Soc.* **2010**, *132*, 6498−6506.
(67) Álvarez-Puebla, R. A. Effects of the Excitation Wavelength on the SERS Spectrum. *J. Phys. Chem. Lett.* **2012**, *3*, 857−866.
(68) Norman, P.; Bishop, D. M.; Jensen, H. J. A.; Oddershede, J. Near-Resonant Absorption in the Time-Dependent Self-Consistent Field and Multiconfigurational Self-Consistent Field Approximations. *J. Chem. Phys.* **2001**, *115*, 10323−10334.
(69) Zhao; Jensen, L.; Schatz, G. C. Pyridine−Ag_{20}Cluster: A Model System for Studying Surface-Enhanced Raman Scattering. *J. Am. Chem. Soc.* **2006**, *128*, 2911−2919.
(70) Chen, H.; Golder, M. R.; Wang, F.; Jasti, R.; Swan, A. K. Raman Spectroscopy of Carbon Nanohoops. *Carbon* **2014**, *67*, 203−213.
(71) Chen, H.; Golder, M. R.; Wang, F.; Doorn, S. K.; Jasti, R.; Tretiak, S.; Swan, A. K. Raman-Active Modes of Even-Numbered Cycloparaphenylenes: Comparisons between Experiments and Density Functional Theory (DFT) Calculations with Group Theory Arguments. *J. Phys. Chem. C* **2015**, *119*, 2879−2887.
(72) Franco, R.; Jacobsen, J. L.; Wang, H.; Wang, Z.; István, K.; Schore, N. E.; Song, Y.; Medforth, C. J.; Shelnutt, J. A. Molecular Organization in Self-Assembled Binary Porphyrin Nanotubes Revealed by Resonance Raman Spectroscopy. *Phys. Chem. Chem. Phys.* **2010**, *12*, 4072−4077.
(73) Duque, J. G.; Chen, H.; Swan, A. K.; Shreve, A. P.; Kilina, S.; Tretiak, S.; Tu, X.; Zheng, M.; Doorn, S. K. Violation of the Condon Approximation in Semiconducting Carbon Nanotubes. *ACS Nano* **2011**, *5*, 5233−5241.
(74) López-Lorente, A. I.; Simonet, B. M.; Valcárcel, M. Raman Spectroscopic Characterization of Single Walled Carbon Nanotubes: Influence of the Sample Aggregation State. *Analyst* **2014**, *139*, 290−298.
(75) Baibarac, M.; Matea, A.; Ilie, M.; Baltog, I.; Magrez, A. Anti-Stokes Raman Spectroscopy as a Method to Identify Metallic and Mixed Metallic/semiconducting Configurations of Multi-Walled Carbon Nanotubes. *Anal. Methods* **2015**, *7*, 6225−6230.
(76) Lefrant, S.; Baibarac, M.; Baltog, I. Raman and FTIR Spectroscopy as Valuable Tools for the Characterization of Polymer and Carbon Nanotube Based Composites. *J. Mater. Chem.* **2009**, *19*, 5690−5704.
(77) Dresselhaus, M. S.; Dresselhaus, G.; Saito, R.; Jorio, A. Raman Spectroscopy of Carbon Nanotubes. *Phys. Rep.* **2005**, *409*, 47−99.
(78) Molina-Duarte, J.; Espinosa-Vega, L. I.; Rodríguez, A. G.; Guirado-López, R. A. Raman Spectra of Single Walled Carbon Nanotubes at High Temperatures: Pretreating Samples in a Nitrogen Atmosphere Improves Their Thermal Stability in Air. *Phys. Chem. Chem. Phys.* **2017**, *19*, 7215−7227.

DOI: 10.1021/acsomega.8b02673
ACS Omega 2018, 3, 16976−16988